

Article

Achieving High Thermal Conductivity and Satisfactory Insulating Properties of Elastomer Composites by Self-Assembling BN@GO Hybrids

Xing Xie ^{1,2} and Dan Yang ^{1,*} 

¹ College of Materials Science and Engineering, Beijing University of Chemical Technology, Beijing 100029, China

² College of New Materials and Chemical Engineering, Beijing Institute of Petrochemical Technology, Beijing 102617, China

* Correspondence: danyang@buct.edu.cn

Abstract: With increasing heat accumulation in advanced modern electronic devices, dielectric materials with high thermal conductivity (λ) and excellent electrical insulation have attracted extensive attention in recent years. Inspired by mussel, hexagonal boron nitride (hBN) and graphene oxide (GO) are assembled to construct mhBN@GO hybrids with the assistance of poly(catechol-polyamine). Then, mhBN@GO hybrids are dispersed in carboxy nitrile rubber (XNBR) latex via emulsion coprecipitation to form elastomer composites with a high λ and satisfactory insulating properties. Thanks to the uniform dispersion of mhBN@GO hybrids, the continuous heat conduction pathways exert a significant effect on enhancing the λ and decreasing the interface thermal resistance of XNBR composites. In particular, the λ value of 30 vol% mhBN@GO/XNBR composite reaches 0.4348 W/(m·K), which is 2.7 times that of the neat XNBR (0.1623 W/(m·K)). Meanwhile, the insulating hBN platelets hinder the electron transfer between adjacent GO sheets, leading to satisfactory electrical insulation in XNBR composites, whose AC conductivity is as low as 10^{-10} S/cm below 100 Hz. This strategy opens up new prospects in the assembly of ceramic and carbonaceous fillers to prepare dielectric elastomer composites with high λ and satisfactory electrical insulation, making them promising for modern electrical systems.



check for updates

Citation: Xie, X.; Yang, D. Achieving High Thermal Conductivity and Satisfactory Insulating Properties of Elastomer Composites by Self-Assembling BN@GO Hybrids. *Polymers* **2023**, *15*, 523. <https://doi.org/10.3390/polym15030523>

Academic Editor: Klaus Werner Stöckelhuber

Received: 26 December 2022

Revised: 13 January 2023

Accepted: 13 January 2023

Published: 19 January 2023



Copyright: © 2023 by the authors. Licensee MDPI, Basel, Switzerland. This article is an open access article distributed under the terms and conditions of the Creative Commons Attribution (CC BY) license (<https://creativecommons.org/licenses/by/4.0/>).

Keywords: thermal conductivity; insulating properties; surface modification; self-assembling; dielectric

1. Introduction

With the high degree of integration and miniaturization of electronic devices, a large amount of heat is accumulated in a small volume of the electronic components in operation. In that regard, efficient heat dissipation has emerged as a critical issue that urgently needs to be addressed to ensure the service life, reliability, and stability of electronic devices [1–4]. Polymeric composites are widely utilized as thermal management materials in electronic packing and engineering due to their excellent characteristics, including high resistivity, low cost, lightweight, and easy processing [5,6]. Elastomers, in particular, are usually used as thermal pads or thermal greases [6–8]. Due to its large amounts of strong polar groups, the carboxy nitrile rubber (XNBR), which shows a relatively high dielectric constant, has been considered as a candidate thermal management material in electron components. Nevertheless, the intrinsic thermal conductivity (λ) of elastomers is usually low (0.16–0.22 W/(m·K)), which does not meet the requirements for heat transfer in advanced electronic components [9–11].

In order to increase the λ of polymers, an effective solution consists of incorporating high thermally conductive fillers into the polymeric matrix, such as ceramics, metals, and carbon materials [2,12,13]. Hexagonal boron nitride (hBN) has attracted considerable

attention from researchers due to its high λ and excellent electrical insulation. Unsatisfactorily, the pristine hBN is poorly compatible with polymers and exhibits a nonuniform dispersion within the polymeric matrix, thereby restraining the growth of λ in the final composites [14,15]. In recent years, the carbonaceous fillers with high electrical conductivity, such as graphene and graphene oxide (GO), have been shown to be able to increase the λ of polymeric composites at a low loading [16]. Nevertheless, the application of such fillers is unavoidably limited in fields where electrical insulation is required. Therefore, designing and preparing dielectric polymeric composites with high λ and outstanding electrical insulation still remain a challenge [17].

Blocking the electron transmission between neighboring carbonaceous fillers by depositing insulating layers or particles is a reliable way to enhance the λ of the polymeric composites while maintaining their electrical insulating properties [15,18]. Shen et al. [15] utilized silica nanoparticles to coat graphene nanoplatelets (GNPs) to construct Silica@GNPs complexes. Then, the obtained Silica@GNPs complexes were incorporated into a polydimethylsiloxane (PDMS) matrix to fabricate Silica@GNP/PDMS composites whose λ value (0.497 W/(m·K)) was found to be 155% that of the neat PDMS (0.195 W/(m·K)). Nevertheless, the electrical resistivity of PDMS composites was still as high as 10^{13} $\Omega\cdot\text{cm}$, ensuring their excellent insulation. Guo et al. [2] first functionalized Al_2O_3 nanoparticles by γ -aminopropyltriethoxysilane (denoted as f- Al_2O_3) and then covered them with GO to form f- Al_2O_3 @RGO hybrids, which were afterward used as thermally conductive fillers for improving the λ of the nanofibrillated cellulose (NFC) matrix. Given the synergistic effect of both Al_2O_3 and RGO, the in-plane λ of the as-prepared f- Al_2O_3 @RGO/NFC composite could be increased to 8.3 W/(m·K) at the RGO and f- Al_2O_3 loadings of 30 wt% and 5.6 wt%, respectively. This result was 2075% of the neat NFC (0.4 W/(m·K)). Meanwhile, the measured electrical resistivity of f- Al_2O_3 @RGO/NFC composites exceeded 10^9 $\Omega\cdot\text{cm}$, thus meeting the requirements for electrical insulation.

Inspired by marine mussels, Messersmith et al. [19] discovered that dopamine containing catechol and amine functional groups can self-polymerize to form strongly adhesive polydopamine (PDA) in the alkaline buffer aqueous solution. Nevertheless, dopamine is unsuitable for widespread use because of its high cost. Therefore, a cheaper substance as a replacement for the expensive dopamine must be found. Luckily, the inexpensive catechol can react with the economical polyamine to synthesize poly(catechol/polyamine) (PCPA) which exhibits adhesion properties similar to PDA [20].

In this work, hBN and GO are assembled to construct mhBN@GO hybrids with the assistance of PCPA to improve the λ of XNBR. Meanwhile, the insulating hBN effectively prevented the connection between adjacent GO sheets, leading to satisfactory electrical insulation for the XNBR composites. The as-prepared XNBR composites might be promising thermal management materials in the future electronic industry.

2. Experimental

2.1. Materials

The XNBR latex (Zeon International Trading Co., Ltd., Tokyo, Japan) was chosen as the polymeric matrix. The hBN platelets were obtained from Dandong Rijin Technology Co., Ltd., Dandong, China. The GO sheets were purchased from Chengdu Organic Chemicals Co., Ltd., Chengdu, China. Polyamine (Tetraethylenepentamine, TEPA) and catechol were provided by Bailingwei Technology Co., Ltd., Beijing, China. Dicumyl peroxide (DCP), tris-acid, and other reagents were produced by Maclean's Reagent Co., Ltd., Beijing, China.

2.2. Preparation Process of mhBN@GO/XNBR Composites

The fabrication method of mhBN@GO/XNBR composites is illustrated in Figure 1. At the beginning, 5 g of hBN were dispersed in 250 mL of deionized water, and the pH of the mixed solution was adjusted to 9.5 with tris-acid. Then, 0.75 g of catechol and 0.25 g of TEPA were added to the above solution and mechanically stirred at 40 °C for 3 h to obtain the modified hBN hybrids (denoted as mhBN). Subsequently, the GO sheets were dispersed

into the blend, which was afterward stirred at 60 °C for 8 h. Finally, the as-obtained mixture was vacuum filtered, washed with deionized water, and vacuum-dried at 60 °C overnight to obtain mhBN@GO hybrids.

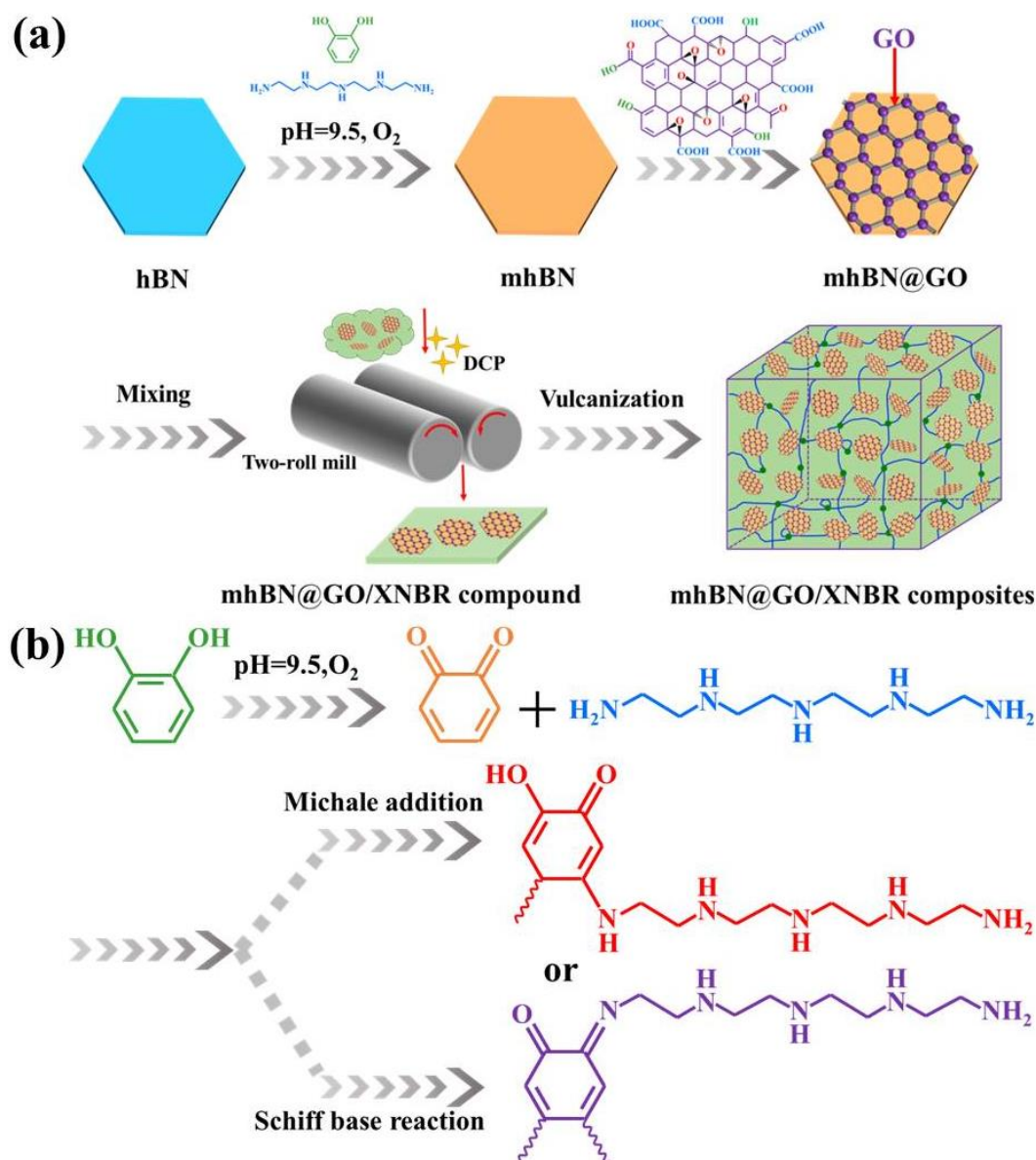


Figure 1. (a) Preparation of mhBN@GO hybrids and mhBN@GO/XNBR composites. (b) The reaction mechanism between catechol and tetraethylenepentamine.

After that, different contents of hBN or mhBN@GO (the volume fractions of 10, 20, and 30 vol%) were incorporated into the XNBR latex via the emulsion coprecipitation method. Initially, the XNBR latex and filler were stirred for 30 min to achieve a uniform dispersion. Then, 1 wt% CaCl₂ was added as a flocculant to the solution. Next, the mixture was water-washed and vacuum-dried at 60 °C to obtain dry compounds. Finally, the compounds and a certain amount of DCP were blended in a double roll open mixer. After 12 h, all as-prepared compounds were compressed by molding at 160 °C and 12 MPa for their vulcanizing time (T_{C90}) to obtain the cured XNBR composites. The T_{C90} values were based on the rheometer (M-3000AU) test data.

2.3. Characterization

The thermogravimetric curves were acquired using a thermogravimetric analysis instrument (TGA, TA SDT650, TA Instruments, New Castle, DE, USA). The surface chemical compositions and surface morphologies of hBN, mhBN, and mhBN@GO were analyzed by means of an X-ray photoelectron spectrometer (XPS, ESCALAB 250, Thermo Electron Corporation, Madison, WI, USA) and a high-resolution transmission electron microscope (HR-TEM, Hitachi H9000, Hitachi Instrument, Tokyo, Japan), respectively. The cross-section morphologies of the XNBR composites were observed by a JSM-5600LV FE-SEM (Thermo Fisher Scientific, Hillsboro, OR, USA). The mechanical properties of the XNBR composites were evaluated using a tensile machine (Instron-3366, Instron Corporation, Norwood, MA, USA). The dielectric behaviors of the composites were studied with a Concept 40 dielectric property tester at room temperature. The λ of the XNBR samples were measured using a flat-panel thermal conductivity meter (DRL-III, Xiangyi Instrument, Xiangtan, China).

3. Results and Discussion

Figure 1a shows the preparation process of the mhBN@GO/XNBR composites. The hBN was first modified by PCPA (denoted as mhBN), which was then assembled with GO to synthesize the mhBN@GO hybrids. Next, the as-prepared mhBN@GO was dispersed into the XNBR matrix to obtain mhBN@GO/XNBR composites via a latex mixing method. A possible reaction mechanism for the PCPA has been added to Figure 1b. First, the catechol was oxidized into quinoid structures in an alkaline tris-acid buffer solution, and then the generated quinoid structures react with polyamine through Michael addition or Schiff base reactions to form an intermolecularly cross-linked PCPA network, which is finally deposited on the surfaces of the hBN platelets [21].

The TGA curves of hBN, mhBN, and mhBN@GO are shown in Figure 2. It can be seen that the hBN displayed a small weight loss in the range of 30–800 °C, which is ascribed to the excellent thermal stability of hBN. However, a slight weight loss of 2.71% was observed in the TGA curve of mhBN at 600 °C. The larger weight loss of mhBN compared with hBN might be attributed to the degradation of the PCPA layer at the high temperature. In addition, there was also a significant weight loss of 11.64% in the TGA curve of mhBN@GO within the range of 30–600 °C. The increased weight loss of mhBN@GO compared with mhBN was due to the pyrolysis of unstable oxygen-containing groups in GO [22].

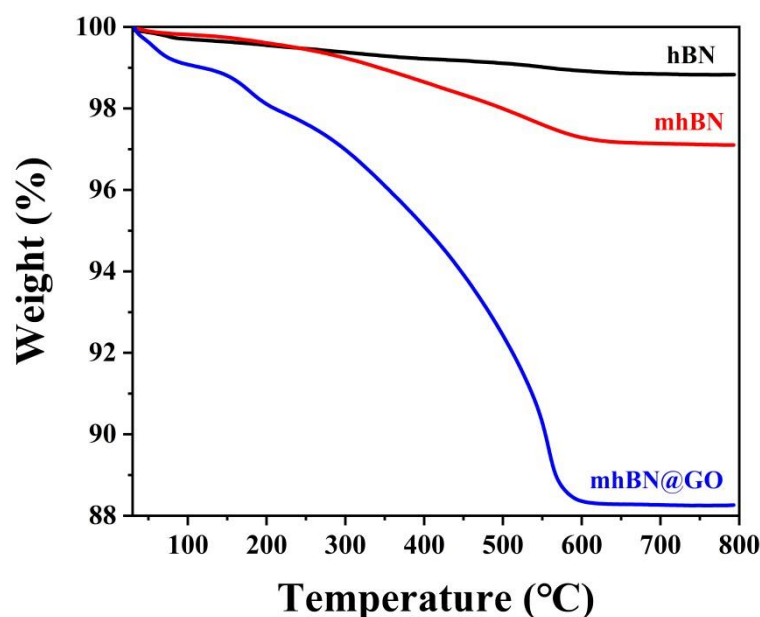


Figure 2. TGA curves of hBN, mhBN, and mhBN@GO.

The surface chemical elements of hBN, mhBN, and mhBN@GO are analyzed via XPS, and the results are shown in Figure 3 and Table 1. The clearly distinguishable peaks were observed in all cases at 191, 285, 398, and 532 eV, which corresponded to boron (B 1s), carbon (C 1s), nitrogen (N 1s), and oxygen (O 1s), respectively. Unexpectedly, the C 1s and O 1s peaks also appeared in the pristine hBN (Figure 3a), which might be due to contamination [23]. Meanwhile, the C 1s core-level spectrum of the hBN was decomposed into three peaks that were attributed to C-C (284.8 eV), C-N (285.5 eV), and C-O (286.6 eV) bonds. However, one new peak corresponding to C=O (288.3 eV) bonds emerged in the mhBN, which was derived from the PCPA coating. In comparison with Figure 3b, another additional peak ascribed to O-C=O (289.4 eV) bonds was observed in mhBN@GO (Figure 3c), which was caused by the -COOH groups in GO. This indicated that the GO could be attached to the mhBN surface through the hydrogen bonds between the -COOH groups in GO and the -OH groups in PCPA [24].

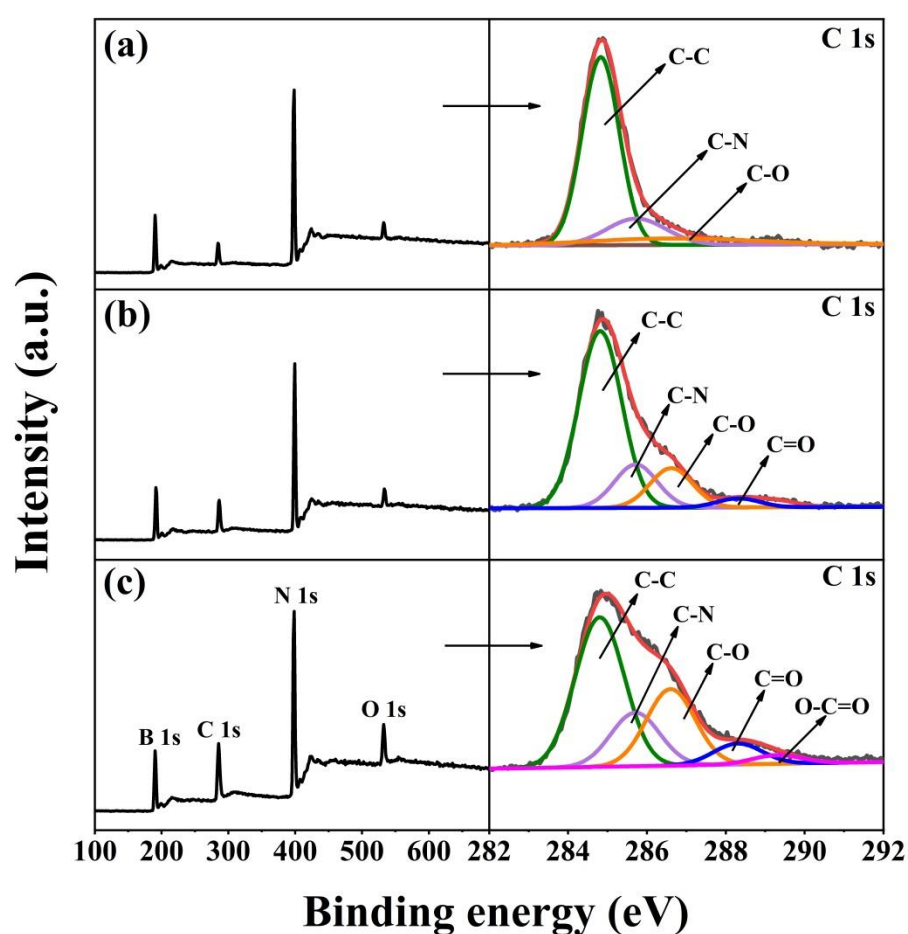


Figure 3. XPS spectra and decomposed C 1s spectra of (a) hBN, (b) mhBN, and (c) mhBN@GO.

Table 1. Chemical element compositions of hBN, mhBN, and mhBN@GO.

Samples	Elemental Analysis (wt%)			
	B	N	C	O
hBN	50.54	39.17	7.79	2.50
mhBN	46.07	38.07	13.03	2.83
mhBN@GO	40.67	34.48	19.31	5.54

Moreover, according to Table 1, the C content in the pristine hBN was only 7.79 wt%, whereas that in mhBN dramatically increased to 13.03 wt%, which was due to the deposition

of PCPA onto the hBN surface [16]. In addition, the content of O increased from 2.50 wt% for hBN to 5.54 wt% for mhBN@GO, which was attributed to the oxygen-containing groups in GO. These results provided compelling evidence of the successful assembly of the PCPA layer and GO sheets on the hBN surface.

Figure 4 displays the HR-TEM images of the hBN, mhBN, and mhBN@GO. In Figure 4a, the pristine hBN exhibited a homogeneous flat surface without any impurities. Compared with Figure 4a, the surface of the mhBN was coated by a smooth layer with a thickness of approximately 5 nm (Figure 4b), which was due to the formation of a PCPA layer on the hBN surface. As shown in Figure 4c, after the introduction of GO, a large and plicate flake was successfully bonded to the surface of mhBN, indicating strong adhesion of PCPA.

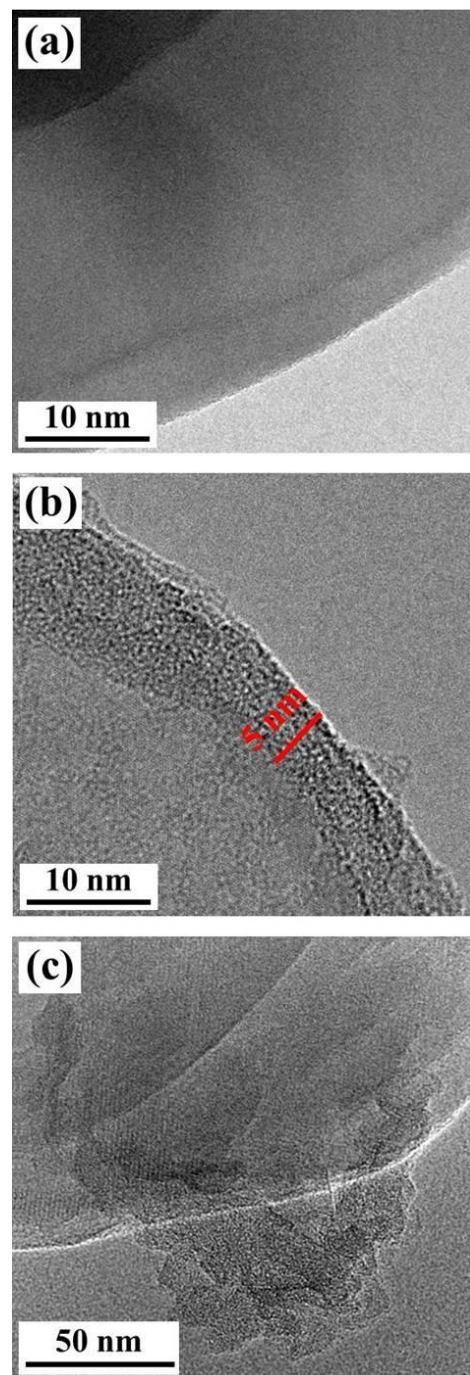


Figure 4. HR-TEM images of (a) hBN, (b) mhBN, and (c) mhBN@GO.

The cross-sectional SEM images of XNBR composites with different filler contents are shown in Figure 5. As seen from Figure 5a–c, multiple hBN platelets were exposed within the XNBR matrix, indicating their poor compatibility and weak interface interaction. Moreover, the number and size of aggregates between hBN platelets in the XNBR matrix increased with the increase in filler content. Compared to the hBN/XNBR composites, the mhBN@GO hybrids were uniformly dispersed in the XNBR matrix according to certain orientations (see the red arrows in Figure 5d–f). These orientations were beneficial for the formation of heat conduction pathways in the XNBR composites. Furthermore, good compatibility and strong interface bonding between the mhBN@GO hybrids and XNBR matrix would be critical in reducing the interface thermal resistance and phonon scattering of elastomer composites [3,25].

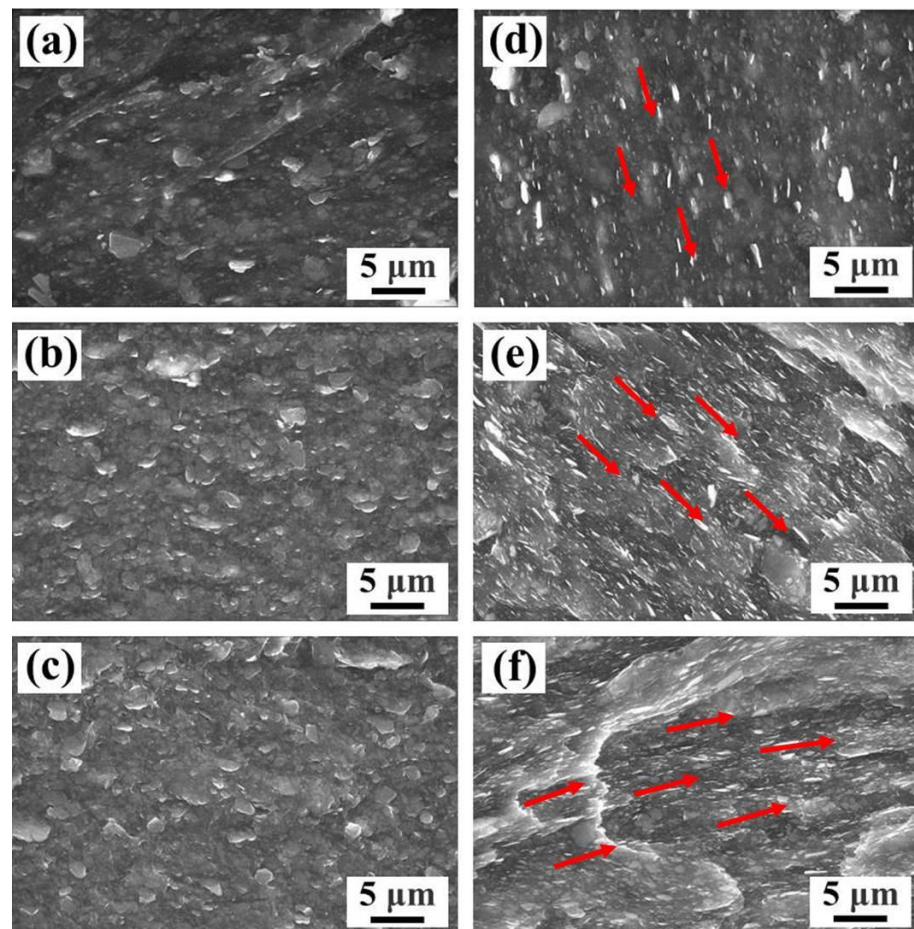


Figure 5. Cross-sectional SEM images of (a) 10 vol% hBN/XNBR, (b) 20 vol% hBN/XNBR, (c) 30 vol% hBN/XNBR, (d) 10 vol% mhBN@GO/XNBR, (e) 20 vol% mhBN@GO/XNBR, and (f) 30 vol% mhBN@GO/XNBR composites. The red arrows represent the orientated dispersion of mhBN@GO.

Figure 6 shows the mechanical properties of XNBR composites filled with various volume fractions of pristine hBN platelets and mhBN@GO hybrids. With the increase in filler content, the tensile strength of both hBN/XNBR and mhBN@GO/XNBR composites increased. However, the tensile strength of mhBN@GO/XNBR composites exceeded that of hBN/XNBR composites at the same filler content. This could be explained by the enforcement effect of mhBN@GO hybrids and the strong interfacial coupling between GO and XNBR [24]. As for the mhBN@GO/XNBR composite with 30 vol% hybrids, the tensile strength increased to 15.35 MPa, which was about 6.50 times that of the neat XNBR (2.36 MPa). Nevertheless, with increasing filler content, the elongation at break of both hBN/XNBR and mhBN@GO/XNBR composites decreased. The mhBN@GO/XNBR composites showed lower elongation at break than the hBN/XNBR composites with the

same filler loading, which could be explained by the following two aspects: first, the strong interface interaction between the mhBN@GO hybrids and XNBR matrix might have restricted the slippage of XNBR chains [26]; secondly, owing to the good dispersion and compatibility of mhBN@GO hybrids in XNBR, the filler networks gradually formed in XNBR composites with the increase in mhBN@GO hybrids content [27,28]. The strong interface bonding between the filler and the matrix and the filler networks in polymeric composites usually leads to a lower elongation at break.

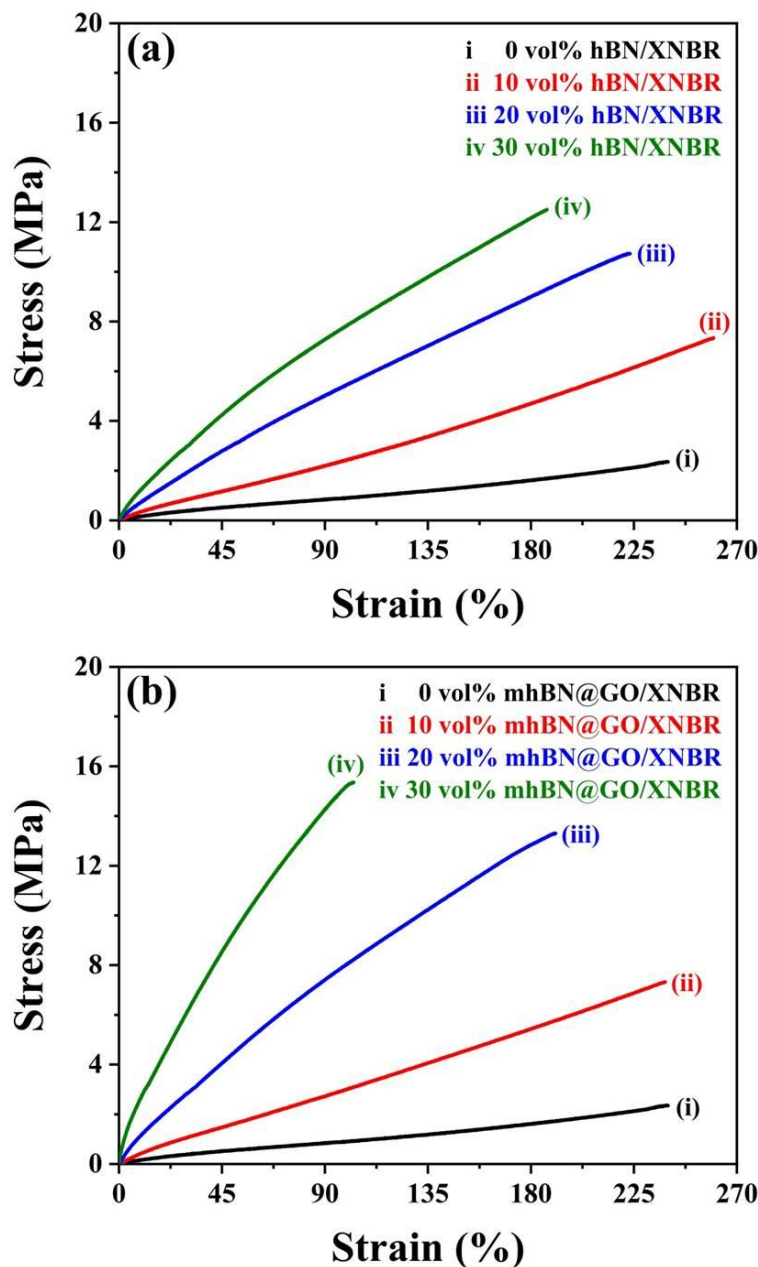


Figure 6. Mechanical properties of (a) hBN/XNBR and (b) mhBN@GO/XNBR composites.

Figure 7 displays the frequency dependence of the dielectric behaviors for neat XNBR and XNBR-based composites over the range of $10\text{--}10^7$ Hz. In Figure 7a,b, the dielectric constant (ϵ_r) of the XNBR composites decreased gradually with increasing frequency. This suggested that the interface polarization between the filler and the XNBR matrix did not have enough relaxation time to catch up with the change in electric field frequency [29]. Besides, the ϵ_r of the XNBR composites decreased with the increase of filler content, which was mainly ascribed to the hBN platelets with a ϵ_r (about 4 at 1 kHz) smaller than that of the

neat XNBR (11.30 at 1 kHz) [30]. However, at the same filler content, the mhBN@GO/XNBR composites displayed a higher ϵ_r than the hBN/XNBR composites (Figure 7a,b). For instance, the ϵ_r of 30 vol% hBN/XNBR composites decreased to 7.13 at 1 kHz, which was inferior to that of 30 vol% mhBN@GO/XNBR composites (8.64 at 1 kHz). This finding could be explained in terms of the following factors. The first was related to the so-called mini-capacitor principle. With the incorporation of GO, many mini-capacitors with GO as electrodes and XNBR as dielectrics are generated in the composites, leading to a high ϵ_r [31,32]. Another one was the enhanced interface polarization between the thermally conductive fillers and the XNBR matrix. The interface polarization in the mhBN@GO/XNBR composites occurred at the interfaces between hBN and PCPA, between PCPA and GO, and between GO and XNBR, whereas that in the hBN/XNBR composites was only between the hBN filler and the XNBR matrix [29].

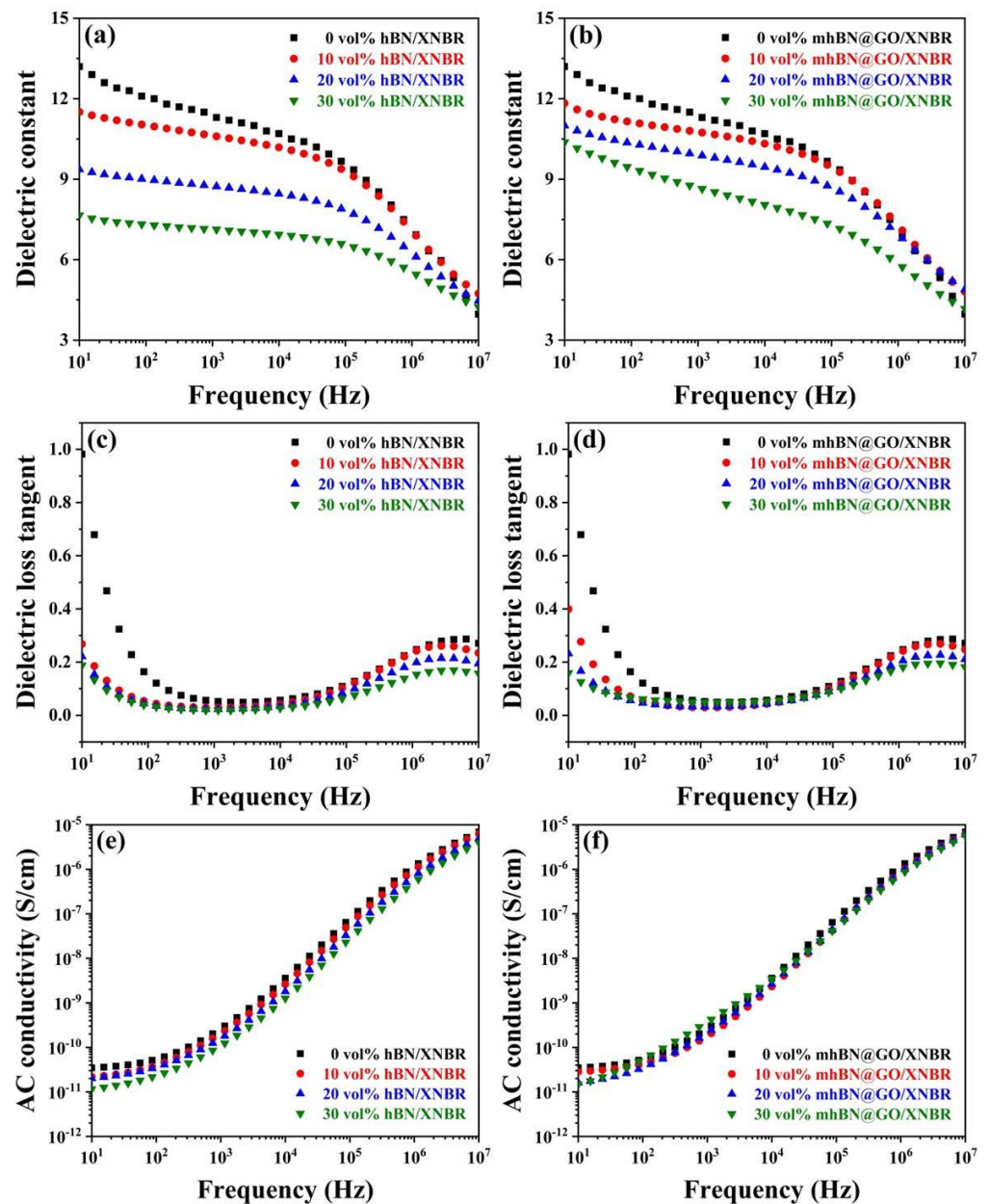


Figure 7. (a,b) Dielectric constant, (c,d) dielectric loss tangent, and (e,f) AC conductivity as functions of frequency for hBN/XNBR and mhBN@GO/XNBR composites, respectively.

The variation of the dielectric loss tangent ($\tan\delta$) with frequency in XNBR composites is shown in Figure 7c,d. The $\tan\delta$ of neat XNBR and XNBR composites first decreases with increasing frequency in the low-frequency range (below 10^3 Hz) and then increases slightly in the high-frequency region (10^3 – 10^7 Hz). The decreased $\tan\delta$ in the low-frequency range could be attributed to Maxwell-Wagner-Sillars (MWS) polarization. However, the slightly increased $\tan\delta$ in the high-frequency region is mainly due to dipolar relaxation [29]. It is evident that the $\tan\delta$ of the hBN/XNBR composites has decreased compared to that of the neat XNBR. This was because the hBN acted as an effective insulator to prevent the space charge and leakage current [33]. With increasing content of mhBN@GO hybrids, the $\tan\delta$ of the mhBN@GO/XNBR composites increased from 0.030 to 0.049 at 1 kHz, which was due to the increased leakage current caused by GO [34]. However, the $\tan\delta$ of hBN/XNBR and mhBN@GO/XNBR composites were still maintained at low levels (<0.1 at 1 kHz), indicating that the mhBN effectively hindered the electrical connection between GO [35].

Figure 7e,f depict the frequency-dependent AC conductivity of XNBR composites. According to Maxwell's equations, the current density $j = \sigma^*E$ and the time derivative of the dielectric displacement $dD/dt = i\omega\varepsilon^*\varepsilon_0E$ are equivalent, where $\sigma^*(\omega)$ is the complex conductivity. Therefore, the conductivity of samples can be calculated according to the following Equations (1) and (2):

$$\sigma^*(\omega) = \sigma'(\omega) + i\sigma''(\omega) = i\omega\varepsilon_0\varepsilon^*(\omega) \quad (1)$$

$$\sigma'(\omega) = \omega\varepsilon_0\varepsilon''(\omega), \sigma''(\omega) = \omega\varepsilon_0\varepsilon'(\omega) \quad (2)$$

where σ^* is the complex conductivity, σ' and σ'' are the real and imaginary parts of the complex conductivity, respectively; ε^* is the complex dielectric function or permittivity, ε' and ε'' are the real and imaginary parts of the complex dielectric function, respectively; ε_0 is the dielectric permittivity of vacuum ($\varepsilon_0 = 8.854 \times 10^{-12}$ F/m), i is imaginary unit $i = \sqrt{-1}$, and ω is the radial frequency [36]. The AC conductivity of XNBR composites increases gradually with increasing frequency over the range of 10 – 10^7 Hz. Obviously, the AC conductivity of the XNBR composites is dependent on the frequency, and it might belong to non-Ohmic conduction [32]. After the addition of hBN or mhBN@GO hybrids, the AC conductivity of the XNBR composites decreased with increasing filler content. The reduction in AC conductivity was mainly due to the lower insulation of the thermally conductive fillers [33]. Notably, the AC conductivity of the XNBR composites was lower than 10^{-10} S/cm below 100 Hz, meaning that the as-prepared mhBN@GO/XNBR composites still maintained excellent electrical insulation [37].

The λ values of the hBN/XNBR and mhBN@GO/XNBR composites are plotted in Figure 8a. It is worth noting that the λ values of the XNBR composites have been gradually enhanced with increasing additions of filler. Moreover, at the same filler loading, the mhBN@GO/XNBR composites exhibited a higher λ compared to that of the hBN/XNBR composites. As the volume fraction of the mhBN@GO hybrids increased to 30%, the corresponding λ increased to 0.4348 W/(m·K), being about 2.7 times of the neat XNBR (0.1623 W/(m·K)). Figure 8b displays the enhancement in λ of XNBR composites relative to that of the neat XNBR. Compared to the hBN/XNBR composites, a stronger λ enhancement could be observed in the mhBN@GO/XNBR composites. The reasons for this difference were as follows: first, the uniform dispersion of the mhBN@GO hybrids and the construction of continuous heat conduction pathways played an essential role in the heat transfer process within the mhBN@GO/XNBR composites; secondly, due to the low interface thermal resistance, the mhBN@GO/XNBR composites exhibited higher efficiently phonon transmission than the hBN/XNBR composites.

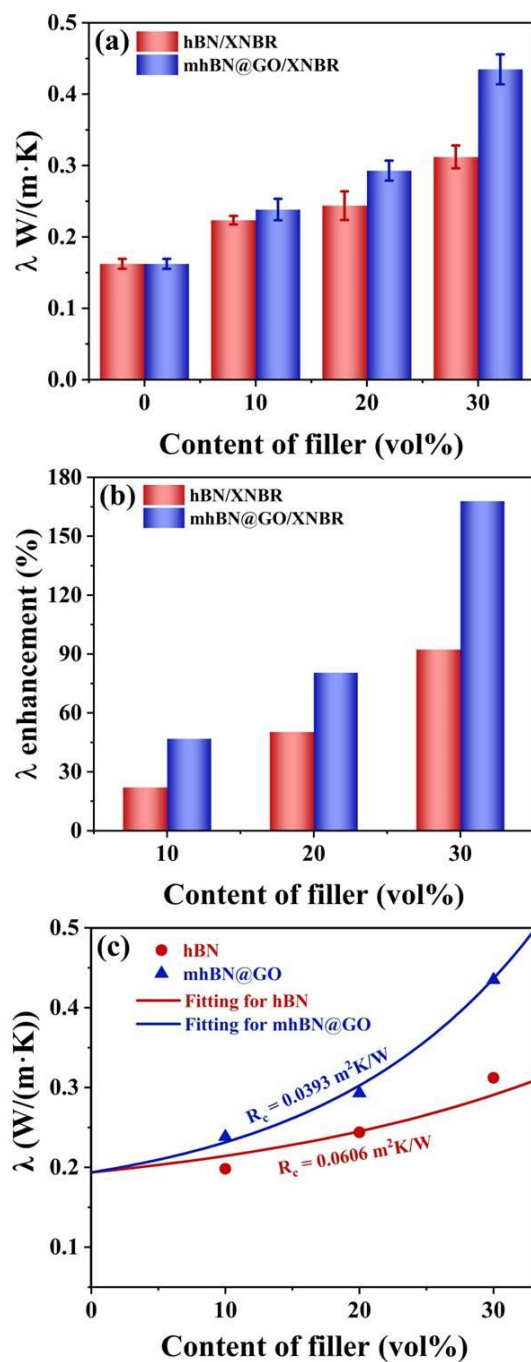


Figure 8. (a) The λ of hBN/XNBR and mhBN@GO/XNBR composites with different filler loading. (b) The enhancement in λ of hBN/XNBR and mhBN@GO/XNBR composites relative to that of the neat XNBR. (c) Fitting λ of hBN/XNBR and mhBN@GO/XNBR composites using the modified Hashin-Shtrikman model.

To expound the internal relationship between the filler and the XNBR matrix, the experimental λ values of XNBR composites (Figure 8c) were fitted using the modified Hashin-Shtrikman model (Equation (3)) [38,39].

$$\lambda_{eff} = \lambda_m \frac{(2KV_f + 1)\lambda_c - (2KV_f - 1)\lambda_m}{(KV_f + 1)\lambda_m - (KV_f - 1)\lambda_c} \quad (3)$$

where λ_m is the λ of the XNBR matrix, λ_c is the λ of the XNBR composites, V_f is the volume fraction of the filler, and K is a coefficient related to the interface thermal resistance of the XNBR composites and defined as Equation (4).

$$K = 13.3347 \exp\left(-13.2701 \frac{R_c \lambda_m}{L}\right) \tag{4}$$

where R_c stands for the interface thermal resistance and L represents the characteristic length of the unit model [3,40]. According to Figure 8c, the interface thermal resistance of the mhBN@GO/XNBR composites ($R_c = 0.0393 \text{ m}^2\text{K/W}$) was lower than that of the hBN/XNBR composites ($R_c = 0.0606 \text{ m}^2\text{K/W}$), demonstrating that PCPA acted as an interface modifier, effectively reducing the interface thermal resistance of XNBR composites.

Figure 9 displays the schematic models of phonon transmission in the hBN/XNBR and mhBN@GO/XNBR composites. In the hBN/XNBR composites, the hBN platelets are inevitably aggregated in the XNBR matrix, leading to severe scattering of phonons and high interface thermal resistance [41]. In addition, ineffective thermal transfer channels are rendered due to poor dispersion of the hBN in the XNBR matrix, limiting the improvement of λ . As a result, the heat transfer process of the hBN/XNBR composites is like a car moving on a mountain road. However, the heat transfer process of the mhBN@GO/XNBR composites is similar to a car speeding on the highway. Because of the reduced interface thermal resistance, the phonons travel along the continuous heat conduction channels with few barriers. In addition, the ordered heat conduction channels formed by mhBN@GO hybrids make the thermal transfer channels shorter [23].

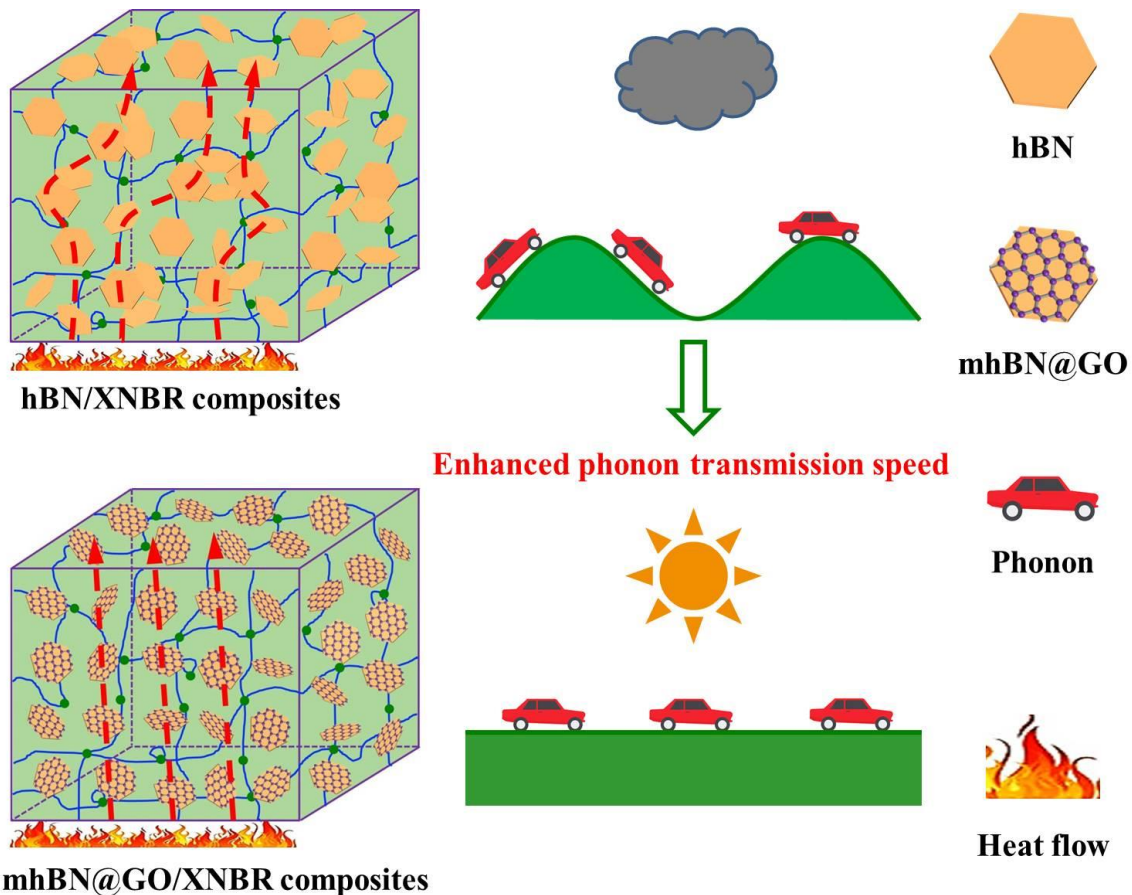


Figure 9. Schematic models of phonon transmission in hBN/XNBR and mhBN@GO/XNBR composites.

4. Conclusions

The thermally conductive mhBN@GO hybrids were successfully synthesized via a facile and green self-assembly method and then were embedded in XNBR latex to obtain high λ and satisfactory insulating properties of mhBN@GO/XNBR composites. Owing to the formation of hydrogen bonds between carboxyl groups in XNBR and hydroxyl groups in GO, the interfacial interaction between the XNBR matrix and mhBN@GO hybrids was obviously improved, leading to reduced interface thermal resistance and the formation of effective thermal transport pathways in the mhBN@GO/XNBR composites. Thus, the obtained mhBN@GO/XNBR composites exhibited a relatively high λ value of 0.4348 W/(m·K), which was 2.7 times that of the neat XNBR (0.1623 W/(m·K)). However, the insulating hBN effectively prevented the connection between adjacent GO sheets, leading to the mhBN@GO/XNBR composites showing a satisfactory electrical insulating property (less than 10^{-10} S/cm below 100 Hz). Therefore, the effective and eco-friendly method proposed in this work allows one to prepare thermal management materials with insulation properties conforming to the heat dissipation requirements for modern electronic devices.

Author Contributions: Date curation, validation, formal analysis, investigation, and writing—original draft, writing—review and editing, X.X. and D.Y.; methodology, funding acquisition, resources, supervision, D.Y. All authors have read and agreed to the published version of the manuscript.

Funding: This research was funded by the National Natural Science Foundation of China (No. 52273259), the Beijing Nova Program (Z201100006820036) from Beijing Municipal Science & Technology Commission, and the Fundamental Research Funds for the Central Universities (buctrc202217), China.

Institutional Review Board Statement: Not Applicable.

Informed Consent Statement: Not Applicable.

Data Availability Statement: Not Applicable.

Conflicts of Interest: The authors declare no conflict of interest.

References

1. Han, J.; Du, G.; Gao, W.; Bai, H. An anisotropically high thermal conductive boron nitride/epoxy composite based on nacre-mimetic 3D network. *Adv. Funct. Mater.* **2019**, *29*, 1900412. [[CrossRef](#)]
2. Guo, S.; Zheng, R.; Jiang, J.; Yu, J.; Dai, K.; Yan, C. Enhanced thermal conductivity and retained electrical insulation of heat spreader by incorporating alumina-deposited graphene filler in nano-fibrillated cellulose. *Compos. Part B Eng.* **2019**, *178*, 107489. [[CrossRef](#)]
3. Guo, Y.; Lyu, Z.; Yang, X.; Lu, Y.; Ruan, K.; Wu, Y.; Kong, J.; Gu, J. Enhanced thermal conductivities and decreased thermal resistances of functionalized boron nitride/polyimide composites. *Compos. Part B Eng.* **2019**, *164*, 732–739. [[CrossRef](#)]
4. Tang, L.; He, M.; Na, X.; Guan, X.; Zhang, R.; Zhang, J.; Gu, J. Functionalized glass fibers cloth/spherical BN filler/epoxy laminated composites with excellent thermal conductivities and electrical insulation properties. *Compos. Commun.* **2019**, *16*, 5–10. [[CrossRef](#)]
5. Xu, X.; Zhou, J.; Chen, J. Thermal transport in conductive polymer-based materials. *Adv. Funct. Mater.* **2020**, *30*, 1904704. [[CrossRef](#)]
6. Niu, H.; Ren, Y.; Guo, H.; Małycha, K.; Orzechowski, K.; Bai, S.-L. Recent progress on thermally conductive and electrical insulating rubber composites: Design, processing and applications. *Compos. Commun.* **2020**, *22*, 100430. [[CrossRef](#)]
7. Xue, Y.; Li, X.; Wang, H.; Zhao, F.; Zhang, D.; Chen, Y. Improvement in thermal conductivity of through-plane aligned boron nitride/silicone rubber composites. *Mater. Des.* **2019**, *165*, 107580. [[CrossRef](#)]
8. Gan, L.; Dong, M.; Han, Y.; Xiao, Y.; Yang, L.; Huang, J. Connection-improved conductive network of carbon nanotubes in a rubber cross-link network. *ACS Appl. Mater. Interfaces* **2018**, *10*, 18213–18219. [[CrossRef](#)]
9. Liu, C.; Wu, W.; Drummer, D.; Shen, W.; Wang, Y.; Schneider, K.; Tomiak, F. ZnO nanowire-decorated Al₂O₃ hybrids for improving the thermal conductivity of polymer composites. *J. Mater. Chem. C* **2020**, *8*, 5380–5388. [[CrossRef](#)]
10. Guo, Y.; Qiu, H.; Ruan, K.; Wang, S.; Zhang, Y.; Gu, J. Flexible and insulating silicone rubber composites with sandwich structure for thermal management and electromagnetic interference shielding. *Compos. Sci. Technol.* **2022**, *219*, 109253. [[CrossRef](#)]
11. Yang, X.; Guo, Y.; Han, Y.; Li, Y.; Ma, T.; Chen, M.; Kong, J.; Zhu, J.; Gu, J. Significant improvement of thermal conductivities for BNNS/PVA composite films via electrospinning followed by hot-pressing technology. *Compos. Part B Eng.* **2019**, *175*, 107070. [[CrossRef](#)]

12. Chen, Y.; Hou, X.; Liao, M.; Dai, W.; Wang, Z.; Yan, C.; Li, H.; Lin, C.-T.; Jiang, N.; Yu, J. Constructing a “pea-pod-like” alumina-graphene binary architecture for enhancing thermal conductivity of epoxy composite. *Chem. Eng. J.* **2020**, *381*, 122690. [[CrossRef](#)]
13. Yang, X.; Fan, S.; Li, Y.; Guo, Y.; Li, Y.; Ruan, K.; Zhang, S.; Zhang, J.; Kong, J.; Gu, J. Synchronously improved electromagnetic interference shielding and thermal conductivity for epoxy nanocomposites by constructing 3D copper nanowires/thermally annealed graphene aerogel framework. *Compos. Part A* **2020**, *128*, 105670. [[CrossRef](#)]
14. Zhang, J.; Du, Z.; Zou, W.; Li, H.; Zhang, C. MgO nanoparticles-decorated carbon fibers hybrid for improving thermal conductive and electrical insulating properties of Nylon 6 composite. *Compos. Sci. Technol.* **2017**, *148*, 1–8. [[CrossRef](#)]
15. Shen, C.; Wang, H.; Zhang, T.; Zeng, Y. Silica coating onto graphene for improving thermal conductivity and electrical insulation of graphene/polydimethylsiloxane nanocomposites. *J. Mater. Sci. Technol.* **2019**, *35*, 36–43. [[CrossRef](#)]
16. Yang, D.; Ni, Y.; Kong, X.; Gao, D.; Wang, Y.; Hu, T.; Zhang, L. Mussel-inspired modification of boron nitride for natural rubber composites with high thermal conductivity and low dielectric constant. *Compos. Sci. Technol.* **2019**, *177*, 18–25. [[CrossRef](#)]
17. Guo, Y.; Wang, S.; Ruan, K.; Zhang, H.; Gu, J. Highly thermally conductive carbon nanotubes pillared exfoliated graphite/polyimide composites. *NPJ Flex. Electron.* **2021**, *5*, 1–9. [[CrossRef](#)]
18. Jiang, F.; Cui, X.; Song, N.; Shi, L.; Ding, P. Synergistic effect of functionalized graphene/boron nitride on the thermal conductivity of polystyrene composites. *Compos. Commun.* **2020**, *20*, 100350. [[CrossRef](#)]
19. Oh, J.; Jo, H.; Lee, H.; Kim, H.-T.; Lee, Y.M.; Ryou, M.-H. Polydopamine-treated three-dimensional carbon fiber-coated separator for achieving high-performance lithium metal batteries. *J. Power Sources* **2019**, *430*, 130–136. [[CrossRef](#)]
20. Dong, X.; Ding, B.; Guo, H.; Dou, H.; Zhang, X. Superlithiated polydopamine derivative for high-capacity and high-rate anode for lithium-ion batteries. *ACS Appl. Mater. Interfaces* **2018**, *10*, 38101–38108. [[CrossRef](#)]
21. Zhu, T.; Chen, Q.; Xie, D.; Liu, J.; Chen, X.; Nan, J.; Zuo, X. Low-cost and heat-resistant poly(catechol/polyamine)-silica composite membrane for high-performance lithium-ion batteries. *ChemElectroChem* **2021**, *8*, 1369–1376. [[CrossRef](#)]
22. Guo, Y.; Yang, X.; Ruan, K.; Kong, J.; Dong, M.; Zhang, J.; Gu, J.; Guo, Z. Reduced graphene oxide heterostructured silver nanoparticles significantly enhanced thermal conductivities in hot-pressed electrospun polyimide nanocomposites. *ACS Appl. Mater. Interfaces* **2019**, *11*, 25465–25473. [[CrossRef](#)]
23. Xiong, S.-W.; Zhang, P.; Xia, Y.; Zou, Q.; Jiang, M.; Gai, J.-G. Unique antimicrobial/thermally conductive polymer composites for use in medical electronic devices. *J. Appl. Polym. Sci.* **2021**, *138*, 50113. [[CrossRef](#)]
24. Wei, Q.; Yang, D.; Yu, L.; Ni, Y.; Zhang, L. Fabrication of carboxyl nitrile butadiene rubber composites with high dielectric constant and thermal conductivity using Al₂O₃@PCPA@GO hybrids. *Compos. Sci. Technol.* **2020**, *199*, 108344. [[CrossRef](#)]
25. Zhang, Z.; Qu, J.; Feng, Y.; Feng, W. Assembly of graphene-aligned polymer composites for thermal conductive applications. *Compos. Commun.* **2018**, *9*, 33–41. [[CrossRef](#)]
26. Xiao, C.; Song, Q.; Shen, Q.; Wang, T.; Xie, W. Understanding on interlaminar nano-reinforcement induced mechanical performance improvement of carbon/carbon composites after silicon infiltration. *Compos. Part B Eng.* **2022**, *239*, 109946. [[CrossRef](#)]
27. Han, Y.; Ruan, K.; Gu, J. Janus (BNNS/ANF)-(AgNWs/ANF) thermal conductivity composite films with superior electromagnetic interference shielding and joule heating performances. *Nano Res.* **2022**, *15*, 4747–4755. [[CrossRef](#)]
28. Cetin, M.S.; Toprakci, H.A.K. Flexible electronics from hybrid nanocomposites and their application as piezoresistive strain sensors. *Compos. Part B Eng.* **2021**, *224*, 109199. [[CrossRef](#)]
29. Yu, L.; Yang, D.; Wei, Q.; Zhang, L. Constructing of strawberry-like core-shell structured Al₂O₃ nanoparticles for improving thermal conductivity of nitrile butadiene rubber composites. *Compos. Sci. Technol.* **2021**, *209*, 108786. [[CrossRef](#)]
30. Ji, S.-Y.; Jung, H.-B.; Kim, M.-K.; Lim, J.-H.; Kim, J.-Y.; Ryu, J.; Jeong, D.-Y. Enhanced energy storage performance of polymer/ceramic/metal composites by increase of thermal conductivity and coulomb-blockade effect. *ACS Appl. Mater. Interfaces* **2021**, *13*, 27343–27352. [[CrossRef](#)]
31. Tawade, B.V.; Apata, I.E.; Singh, M.; Das, P.; Pradhan, N.; Al-Enizi, A.M.; Karim, A.; Raghavan, D. Recent developments in the synthesis of chemically modified nanomaterials for use in dielectric and electronics applications. *Nanotechnology* **2021**, *32*, 142004. [[CrossRef](#)] [[PubMed](#)]
32. Wang, R.; Xie, C.; Luo, S.; Xu, H.; Gou, B.; Zeng, L. Preparation and properties of MWCNTs-BNNSs/epoxy composites with high thermal conductivity and low dielectric loss. *Mater. Today Commun.* **2020**, *24*, 100985. [[CrossRef](#)]
33. Hu, B.; Guo, H.; Wang, Q.; Zhang, W.; Song, S.; Li, X.; Li, Y.; Li, B. Enhanced thermal conductivity by constructing 3D-networks in poly(vinylidene fluoride) composites via positively charged hexagonal boron nitride and silica coated carbon nanotubes. *Compos. Part A: Appl. Sci. Manuf.* **2020**, *137*, 106038. [[CrossRef](#)]
34. Wang, B.; Yin, X.H.; Peng, D.; Lv, R.H.; Na, B.; Liu, H.S.; Gu, X.B.; Wu, W.; Zhou, J.L.; Zhang, Y. Achieving thermally conductive low loss PVDF-based dielectric composites via surface functionalization and orientation of SiC nanowires. *Express Polym. Lett.* **2020**, *14*, 2–11. [[CrossRef](#)]
35. Hao, Y.; Li, Q.; Pang, X.; Gong, B.; Wei, C.; Ren, J. Synergistic enhanced thermal conductivity and dielectric constant of epoxy composites with mesoporous silica coated carbon nanotube and boron nitride nanosheets. *Materials* **2021**, *14*, 5251. [[CrossRef](#)]
36. Schönhal, A.; Kremer, F. *Analysis of Dielectric Spectra*; Springer: Berlin/Heidelberg, Germany, 2003; pp. 59–98.
37. Shen, Z.; Feng, J. Achieving vertically aligned SiC microwires networks in a uniform cold environment for polymer composites with high through-plane thermal conductivity enhancement. *Compos. Sci. Technol.* **2019**, *170*, 135–140. [[CrossRef](#)]

38. Ngo, I.L.; Byon, C.; Lee, B.J. Analytical study on thermal conductivity enhancement of hybrid-filler polymer composites under high thermal contact resistance. *Int. J. Heat Mass Transf.* **2018**, *126*, 474–484. [[CrossRef](#)]
39. Ngo, I.L.; Vattikuti, P.S.V.; Byon, C. A modified Hashin-Shtrikman model for predicting the thermal conductivity of polymer composites reinforced with randomly distributed hybrid fillers. *Int. J. Heat Mass Transf.* **2017**, *114*, 727–734. [[CrossRef](#)]
40. Liu, X.; Gao, Y.; Shang, Y.; Zhu, X.; Jiang, Z.; Zhou, C.; Han, J.; Zhang, H. Non-covalent modification of boron nitride nanoparticle-reinforced PEEK composite: Thermally conductive, interfacial, and mechanical properties. *Polymer* **2020**, *203*, 122763. [[CrossRef](#)]
41. Du, C.; Li, M.; Cao, M.; Song, S.; Feng, S.; Li, X.; Guo, H.; Li, B. Mussel-inspired and magnetic co-functionalization of hexagonal boron nitride in poly(vinylidene fluoride) composites toward enhanced thermal and mechanical performance for heat exchangers. *ACS Appl. Mater. Interfaces* **2018**, *10*, 34674–34682. [[CrossRef](#)]

Disclaimer/Publisher's Note: The statements, opinions and data contained in all publications are solely those of the individual author(s) and contributor(s) and not of MDPI and/or the editor(s). MDPI and/or the editor(s) disclaim responsibility for any injury to people or property resulting from any ideas, methods, instructions or products referred to in the content.